PCCP

PAPER

View Article Online
View Journal | View Issue

Acoustic phonons and negative thermal expansion in MOF-5

Leila H. N. Rimmer,†[a] Martin T. Dove,*[ab] Andrew L. Goodwin[c] and David C. Palmer[d]

Cite this: *Phys. Chem. Chem. Phys.*, 2014, **16**, 21144

Received 18th April 2014,
Accepted 29th July 2014

DOI: 10.1039/c4cp01701c

www.rsc.org/pccp

The mechanism of negative thermal expansion (NTE) in MOF-5 has been studied using a rigid unit mode analysis of the phonons responsible for NTE. In addition to confirming the role of the previously proposed optic 'trampoline mode' mechanism [Lock *et al.*, *Dalton Trans.*, 2013, **42**, 1933–2320], we have identified a new *acoustic* mode mechanism that makes a major contribution to the macroscopic NTE of this framework.

1 Introduction

Negative thermal expansion—the unusual phenomenon in which a material will *shrink* rather than expand on increasing temperature—is a property which has attracted increasing interest in recent years. The review of Lind[1] identifies a large and systematic rise in the number of studies of negative thermal expansion (NTE) in the two decades after 1990. Much of this work has been carried out on ceramic materials as described by Lind[1] and, in another review, by Romao *et al.*[2] The structures of many of these materials can be described as frameworks or networks of linked polyhedral groups of atoms—potentially a critical feature in any NTE mechanism.[3,4] One example of this description is the network of corner-linked WO_4 tetrahedra and ZrO_6 octahedra in ZrW_2O_8.

Less effort has been devoted to understanding NTE in metal–organic framework (MOF) materials, which can be described as nano-porous frameworks composed of cations connected *via* molecular ligands. One simple example exhibiting NTE is $Zn(CN)_2$,[5,6] in which the Zn^{2+} cations are tetrahedrally coordinated with the CN^- molecular ions forming the linkages between tetrahedra in a manner analogous to the O^{2-} anion in silicates.

MOF-5, Zn_4O(1,4-benzenedicarboxylate), is one of the more important MOFs that exhibit NTE. Moreover, its crystal structure[7] has cubic symmetry, meaning that the NTE is isotropic. The crystal structure of MOF-5, illustrated in Fig. 1, consists of Zn_4O_{13} clusters arranged as four ZnO_4 units with a shared oxygen atom; separated clusters are linked by benzenedicarboxylate (BDC) ligands. MOF-5 has a large volumetric coefficient of NTE that has been measured as $\alpha_V \approx -48$ M K^{-1}.[8]

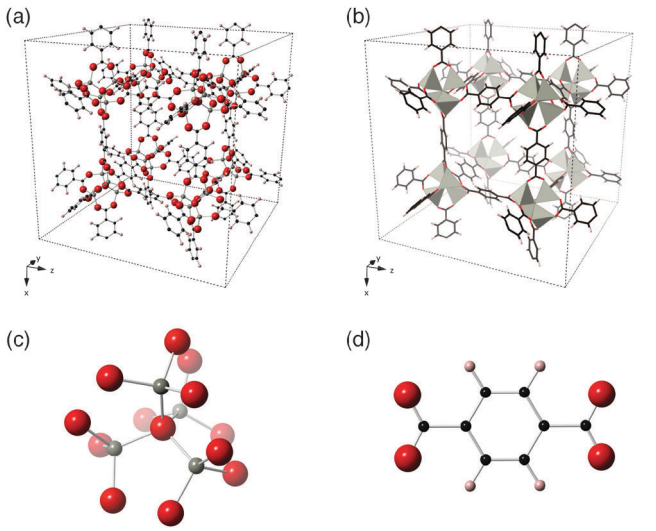

Fig. 1 The MOF-5 structure. (a) Shows MOF-5 in ball-and-stick format. Red atoms are O, grey atoms are Zn, black atoms are C and pink atoms are H. (b) Shows MOF-5 in terms of ZnO_4 tetrahedra linked by BDC ligands. Grey tetrahedra are ZnO_4. Unit cells (with cubic cell parameter a = 25.909) are shown as dashed black lines. This material has space group $Fm\bar{3}m$. (c) Shows the ZnO_4 unit in further detail. The four ZnO_4 units are connected by a single shared O atom at the centre of the cluster. (d) Shows the BDC ligand in further detail. Two carboxylate groups exist at either end of the aromatic ring.

[a] *Department of Earth Sciences, University of Cambridge, Downing Street, Cambridge CB2 3EQ, UK*
[b] *School of Physics & Astronomy and Materials Research Institute, Queen Mary University of London, Mile End Road, London E1 4NS, UK. E-mail: martin.dove@qmul.ac.uk*
[c] *Inorganic Chemistry Laboratory, Department of Chemistry, University of Oxford, South Parks Road, Oxford, OX1 3QR, UK*
[d] *CrystalMaker Software Limited, Centre for Innovation & Enterprise, Oxford University Begbroke Science Park, Woodstock Road, Begbroke, Oxfordshire, OX5 1PF, UK*
† Present address: School of Physics & Astronomy and Materials Research Institute, Queen Mary University of London, Mile End Road, London E1 4NS, U.K, and CrystalMaker Software Limited, Centre for Innovation & Enterprise, Oxford University Begbroke Science Park, Woodstock Road, Begbroke, Oxfordshire, OX5 1PF, UK.

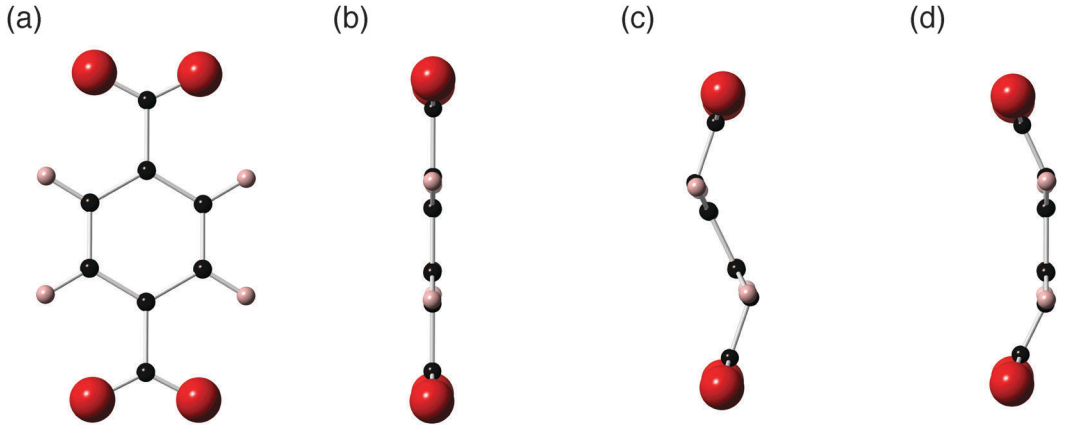

Fig. 2 Illustration of the 'trampoline' mode thought to be responsible for NTE in MOF-5. (a) Shows the original BDC ligand. (b) Shows a side-view of the same ligand. (c) Shows a vibration that minimises deformation of the carboxylate and benzene groups. Whilst it reduces the length of the ligand and is low energy because it minimises deformation of those units, it is not the lowest energy deformation of its type. (d) Shows another vibration that minimises deformation of the carboxylate and benzene groups involving translation of the benzene ring; the 'trampoline mode' thought to drive NTE in MOF-5. Whilst the length of the ligand is decreased, the overall deformation undergone by the BDC ligand is minimised and so this NTE mode can exist at extremely low frequency.

Like most NTE frameworks, the thermal expansion of MOF-5 is thought to be driven by its atomic-scale vibrational modes. Phonons normally drive positive thermal expansion (PTE) since the anharmonicity of a typical interatomic potential leads to longitudinal thermal expansion of bonds. This, in turn, contributes to expansion of the material at the macroscopic level as temperature increases. However, in some framework materials, the energy cost of bond angle bending is much less than that of longitudinal bond stretching. When this is the case, a phonon consisting of transverse vibrations and negligible longitudinal bond stretching can act to 'pull in' surrounding atoms which, in turn, contributes to contraction of the material at the macroscopic level.[1,2]

Overall thermal expansion is dependent on the balance between NTE-contributing and PTE-contributing phonons. Phonon amplitude, and thus the degree to which a given phonon helps drive NTE, is inversely proportional to the square of vibrational frequency.[9] If NTE phonons exist at sufficiently low frequency and, if they account for a sufficiently large proportion of the full phonon spectrum, they can outweigh the standard PTE modes and result in macroscopic NTE. Since phonons are cooperative excitations that involve the whole system (and not just local flexing of the structure) the question of whether NTE phonons can have sufficiently low frequency is one of whether the local flexibility associated with bond bending extends across the whole crystal. The Rigid Unit Mode model[10–12] is one way to understand the origin of the structural flexibility necessary for NTE.[3,4] The essential idea is that a set of phonons—called *rigid unit* modes (RUMs)—can propagate with negligible deformation of coordination polyhedra or similar units, thereby corresponding to low-energy flexing of the whole structure. Not only do RUMs inherently describe the transverse bond vibrations that are proposed as the mechanism of NTE, but they also provide the link between local flexibility and the 'whole crystal' flexibility that is required to produce sufficiently low energy NTE phonons.

In the case of MOF-5, *ab initio* lattice dynamics calculations of Γ-point optic phonons[8] found that MOF-5 has a large number of modes with frequency below 5.4 THz. Many of these were found to drive NTE and were identified as RUMs involving transverse vibrations of rigid ZnO_4 tetrahedra, carboxylate triangles and benzene hexagons. The lowest frequency NTE phonons were those that involve flexing of the BDC ligand[8,13]—see Fig. 2.

The proposal that NTE in MOF-5 is driven by flexing of the BDC ligand was later supported by analysis of thermal displacement parameters determined from X-ray diffraction.[13] A further in-depth experimental study, combining X-ray and neutron diffraction, inelastic neutron scattering (INS), EXAFS and *ab initio* molecular dynamics (all examined as a function of temperature)[14] confirmed that this mode, which was termed a 'trampoline mode', is prevalent in the lowest-energy optic phonons. It was therefore concluded that this mode drives the NTE in MOF-5.

Despite these studies, our understanding of NTE in MOF-5 is far from complete. In order to fully understand NTE behaviour, contributions from *all* phonons must be considered—therefore the entire Brillouin zone must be investigated. Although the INS study was able to capture phonon information for most of the Brillouin zone, this particular spectroscopy technique struggles to capture very low frequencies and does not contain information relating to phonon wave vector. In addition, although *ab initio* phonons have previously been calculated for some of the high-symmetry Brillouin zone directions in MOF-5,[15] detailed analysis has only been carried out for phonons at zero wave vector. Given the complexity of the phonon spectrum of a MOF material, we must also have a means of systematically determining whether identified NTE phonons do indeed correspond to the 'trampoline mode' or to other similar modes.

Our approach to this problem, and one which we have previously applied to simpler NTE materials with some success,[6,17] is to map phonons calculated for simple models of framework flexibility (which, in turn, simulate different types of RUM) onto

results from calculations of *ab initio* phonon dispersion curves. The degree to which each simple model can reproduce the NTE-driving phonons in the *ab initio* phonon spectrum tells us the type of atomic-scale motion that ultimately drives the NTE in this material.

2 Methodology

2.1 *Ab initio* lattice dynamics and mode Grüneisen parameters

Ab initio calculations of the structure and lattice dynamics of MOF-5 were carried out using Density Functional Theory (DFT) using plane-wave basis sets and representing the effects of core electrons using the standard pseudopotential method. We used the CASTEP program[18] for this work, with the GGA-PBE functional[19,20] and CASTEP's internal on-the-fly-generated pseudopotentials for Zn, O, C and H, regenerated so as to be norm-conserving. The material was explicitly defined as an insulator for all calculations. For geometry optimisation calculations, empirical dispersion corrections were applied according to the Grimmé scheme.[21] Forces, stresses and dielectric constants were converged to within 0.005 eV $Å^{-1}$, 0.01 GPa and 0.0001 respectively. This was achieved using a plane wave cutoff energy of 950 eV and a single wave-vector for the integration of electronic states across the Brillouin zone. Geometry optimisation at 0 GPa gave final structural parameters as detailed in Table 1.

Phonons were calculated in CASTEP using Density-Functional Perturbation Theory (DFPT)[22] with a 2 × 2 × 2 Monkhorst–Pack[23] grid. LO/TO splitting was explicitly accounted for and the acoustic sum rule was enforced. Fourier interpolation was used to calculate phonons along high-symmetry directions[24–28] for the production of dispersion curves. In addition, phonons were calculated for 471 wave-vectors spaced randomly throughout the Brillouin zone for the production of the vibrational density of states.

The structural relaxation and phonon calculation were repeated for a second unit cell, this time with cell parameters fixed at values 0.1% larger than their 0 GPa counterpart. Comparison of the phonon frequencies for the two volumes allowed calculation of the individual mode Grüneisen parameters $\gamma_{i,\mathbf{k}}$, defined as

$$\gamma_{i,\mathbf{k}} = -\frac{\partial \ln \omega_{i,\mathbf{k}}}{\partial \ln V} \quad (1)$$

where $\omega_{i,\mathbf{k}}$ is the angular frequency of the phonon mode i with wave vector $\mathbf{k}$, and V is the volume. Essentially $\gamma_{i,\mathbf{k}}$ quantifies the relative change in phonon frequency for a relative change in volume. Provided that intrinsic anharmonic effects are not too large, the mode Grüneisen parameters determine the value of the volumetric coefficient of thermal expansion $\alpha_V = \partial \ln V/\partial T$ through the relation

$$\alpha_V = \frac{\bar{\gamma} C_V}{BV} \quad (2)$$

where T is temperature, B is the bulk modulus and C_V is the constant-volume heat capacity. $\bar{\gamma}$ is known as the overall Grüneisen parameter, defined as

$$\bar{\gamma} = \frac{1}{C_V} \sum_{i,\mathbf{k}} \gamma_{i,\mathbf{k}} \hbar \omega_{i,\mathbf{k}} \frac{\partial n(\omega_{i,\mathbf{k}}, T)}{\partial T} \quad (3)$$

where $\hbar$ is the reduced Planck's constant and n is the Bose–Einstein distribution defined as

$$n(\omega, T) = \frac{1}{(\exp(\hbar\omega/k_B T) - 1)} \quad (4)$$

where k_B is Boltzmann's constant.

From this formalism we see that NTE phonons have negative values of $\gamma_{i,\mathbf{k}}$; that is, the frequencies of NTE phonons *increase* with volume expansion. If these phonons constitute a sufficient part of the sum in eqn (3), the overall Grüneisen parameter will have a negative value and hence (from eqn (2)) the value of α_V will be negative.

At this stage one limitation of the *ab initio* calculations must be made clear: whilst the parameterised dispersion correction term can be added to most DFT-calculated values, dispersion corrections are currently not implemented for DFPT phonon calculations. Dispersion correction *is* possible when using a finite-displacement method (and has been achieved for the MOF ZIF-8,[29] though not yet for MOF-5[8,13,15]) but this approach is only suitable for Γ-point calculations since a converged 'supercell method' calculation is not feasible for a material of this size.

As this investigation requires consideration of the entire phonon spectrum, it was decided to proceed with relaxations using dispersion corrected DFT but, for the phonon calculation itself, to proceed with DFPT despite its lack of dispersion correction. Although the phonons would not be as accurate as desired, we anticipated that they would nevertheless provide valuable insight. More specifically, Fig. 1 shows that the BDC ligands in MOF-5 are not in close contact (nearest neighbour benzene rings are ~16 Å apart), meaning that the effect of van der Waals interactions on phonons would ultimately be small. Our study, in any event, provides the first detailed NTE examination of low frequency phonons away from the Γ point, a region of the vibrational spectrum not previously covered in-depth.

Table 1 Structural data for the MOF-5 equilibrium cell as optimised at 0 GPa *via* DFT with dispersion correction in CASTEP. Experimental data obtained for evacuated MOF-5 *via* neutron diffraction at 0 GPa, 3.5 K is shown alongside for comparison. As can be clearly seen, the *ab initio* results are very close to the experimentally-derived values

	This study (DFT + dispersion correction)			Neutron diffraction at 3.5 K[16]		
Space group	225 ($Fm\bar{3}m$)			225 ($Fm\bar{3}m$)		
Cell parameter	a = 26.058			a = 25.909		
Atom	x	y	z	x	y	z
H	0.3080	0.3080	0.0479	0.3087	0.3087	0.0483
C	0.8892	0.2500	0.2500	0.8882	0.2500	0.2500
C	0.5535	0.2500	0.2500	0.5533	0.2500	0.2500
C	0.2173	0.2173	0.0266	0.2174	0.2174	0.0267
O	0.2500	0.2500	0.2500	0.2500	0.2500	0.2500
O	0.7806	0.7806	0.8671	0.7807	0.7807	0.8667
Zn	0.2063	0.2063	0.2063	0.2061	0.2061	0.2061

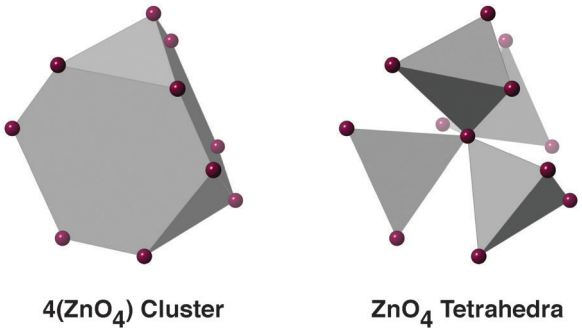

Fig. 3 Flexibility models of the inorganic unit. Grey polyhedra represent rigid units, purple spheres represent flexible linkages.

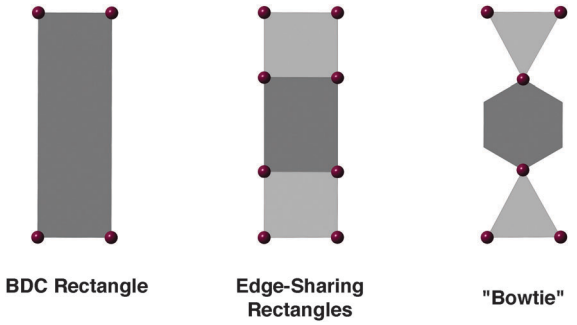

Fig. 4 Flexibility models of the BDC ligand. Grey polyhedra represent rigid units, purple spheres represent flexible linkages.

2.2 MOF-5 rigid unit models

Given previous work had already shown that ZnO_4 tetrahedra undergo negligible deformation at low energy,[14] models involving such deformations were not considered for this investigation. Instead, the inorganic Zn_4O_{13} clusters were represented by one of,

(1) A single rigid cluster.

(2) Four rigid ZnO_4 tetrahedra, connected by a single shared oxygen atom about which each tetrahedron has flexibility to rotate.

The BDC ligands were represented by one of,

(1) A rigid BDC rectangle.

(2) Three rigid edge-sharing rectangles hinged where carboxylates and benzene rings meet.

(3) A rigid benzene hexagon with rigid carboxylate triangles connected at either end (*i.e.* a 'bowtie' shape).

Illustrations of each of these rigid units can be found in Fig. 3 and 4.

Rigid unit models for this material were created and analysed using our program CRUSH,[10,30] which carries out molecular lattice dynamics calculations on structures made up of interconnected rigid units.‡ Calculated phonons with zero frequency correspond to RUMs of the investigated structure whilst phonons with non-zero frequency correspond to modes that involve distortions of those rigid units. Taking into account all possible combinations of the MOF-5 rigid units represented here, a total of six different models were constructed in CRUSH for the 0 GPa MOF-5 cell and phonons were calculated.

Our approach to analyse the RUM flexibility of a material is to quantify the extent to which the phonon eigenvectors can be matched to the RUM eigenvectors. To quantify this match we define a dimensionless 'match' coefficient, $m_{i,\mathbf{k}}$, as

$$m_{i,\mathbf{k}} = \Omega^2 \sum_j \frac{\mathbf{e}_{i,\mathbf{k}}^{\text{phonon}} \cdot \mathbf{e}_{j,\mathbf{k}}^{\text{model}}}{\Omega^2 + {\omega_{j,\mathbf{k}}}^2} \quad (5)$$

where $\mathbf{e}_{i,\mathbf{k}}^{\text{phonon}}$ is the eigenvector of the *ab initio* phonon mode i at wave vector $\mathbf{k}$, $\mathbf{e}_{j,\mathbf{k}}^{\text{model}}$ is the eigenvector of the CRUSH mode j at the same wave vector $\mathbf{k}$ and $\omega_{j,\mathbf{k}}$ is the corresponding angular frequency of the CRUSH-calculated phonon j. Ω is a scale factor that avoids division-by-zero errors when $\omega = 0$.

By setting Ω equal to 1 THz, a value of ${\omega_{j,\mathbf{k}}}^2 = 0$ gives a values of $1/(\Omega^2 + {\omega_{j,\mathbf{k}}}^2) = 1\ \text{THz}^{-2}$, which sets the scale of $m_{i,\mathbf{k}}$ values to range from 0 to 1. A value close to 1 implies that the *ab initio* phonon i is a close match for a RUM. A value close to 0 implies that the *ab initio* phonon i involves significant distortions of the rigid units described in the rigid unit model in question (*i.e.* either it is a poor match for any CRUSH mode, or else it only matches CRUSH phonons which involve non-trivial distortions of the rigid units). $m_{i,\mathbf{k}}$, therefore, represents the degree to which the rigid unit model in question is able to reproduce the mode i at the wave vector $\mathbf{k}$.

‡ The latest version of CRUSH can be obtained from the corresponding author.

3 Results

3.1 NTE phonons in MOF-5

The full phonon density of states calculated for MOF-5 is shown in Fig. 5a. Fig. 5b shows the same density of states replotted with a colour scale that represents the average value of $\gamma_{i,\mathbf{k}}$ within each bin. These results show that NTE phonons (those with negative values of $\gamma_{i,\mathbf{k}}$) exist with frequencies from zero to 8 THz; this upper value is higher than those observed in previous *ab initio* studies.[8]

Fig. 6 shows phonon dispersion curves and densities of states in the 0–8 THz frequency range. Fig. 6a shows the complete set of dispersion curves in this frequency range whilst Fig. 6b shows the same dispersion curves shaded according to the value of $\gamma_{i,\mathbf{k}}$ using the same scale as for the density of states plotted in Fig. 5b. The strongest contribution to NTE comes from acoustic modes in the Γ–X–W region and a very low frequency optic mode ($\sim$0.5 THz) that spans the entire Brillouin zone. The acoustic NTE modes have $\gamma_{i,\mathbf{k}} \sim -45$ around X and W, rising to ~ -20 around Γ and to ~ -4 elsewhere. Meanwhile, the optic mode has $\gamma_{i,\mathbf{k}} \sim -30$ throughout the Brillouin zone.

For the modes with higher frequencies, $\gamma_{i,\mathbf{k}}$ rises to ~ 0 at a frequency of around 1.1 THz. There is then a single, weak, PTE mode ($\gamma_{i,\mathbf{k}} \sim 1$ at 1.2 THz) before $\gamma_{i,\mathbf{k}}$ falls to a value ~ -15 by 1.6 THz. It then starts to rise again with increasing frequency, becoming very small above 2.6 THz and reaching ~ 0 by 5.4 THz. There are some weak PTE phonons ($\gamma_{i,\mathbf{k}} \sim 1$) at 5.4–7.6 THz,

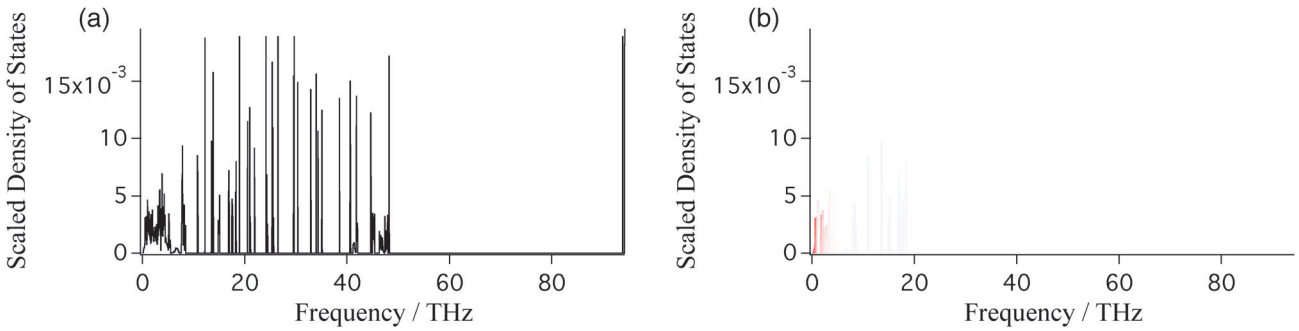

Fig. 5 (a) Full MOF-5 vibrational density of states. (b) The same histogram, shaded according to the average value of $\gamma_{i,\mathbf{k}}$ for each bin; the colour scale ranges from red for $\gamma_{i,\mathbf{k}} \leq -40$ to white for $\gamma_{i,\mathbf{k}} = 0$ through to blue for $\gamma_{i,\mathbf{k}} \geq +40$. For the sake of clarity, this graph omits a black outline to the histogram. Note that (b) appears almost featureless above 20 THz, indicating that $\gamma_{i,\mathbf{k}} \approx 0$ above this frequency. These two graphs show that the NTE phonons in MOF-5 are found in the 0–8 THz region of the frequency spectrum.

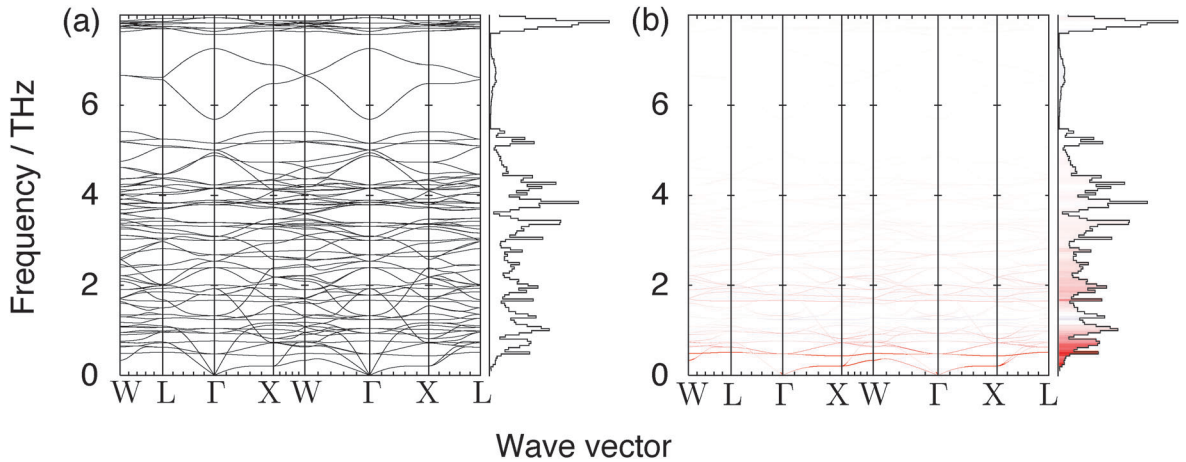

Fig. 6 (a) Phonon dispersion curves and full Brillouin zone density of states for the equilibrium MOF-5 cell. Wave vectors for points in the Brillouin zone of high symmetry are labelled according to the notation of Bradley and Cracknell.[31] With respect to the conventional face-centred cubic cell, Γ = (0,0,0), X = (1,0,0), L = (0.5,0.5,0.5) and W = (0.5,1,0). (b) Shows the same data shaded according to the value of $\gamma_{i,\mathbf{k}}$ of each mode at each wave vector with respect to phonons calculated for a MOF-5 cell with an 0.1% larger volume. The colour scale ranges from red ($\gamma_{i,\mathbf{k}} \leq -40$) to white ($\gamma_{i,\mathbf{k}} = 0$) through to blue ($\gamma_{i,\mathbf{k}} \geq +40$). Bins that make up the density of states are shaded according to the average $\gamma_{i,\mathbf{k}}$ for each bin using the same colour scale.

followed by the final band of weak NTE phonons ($\gamma_{i,\mathbf{k}} \sim -1$) at 7.9 THz. These last NTE phonons have not been noted in any previous studies.[8,13,14]

Returning to the lowest frequency phonons in MOF-5, we have quantified the relative importance of the acoustic modes and optic mode at ~0.5 THz for NTE through computing the overall Grüneisen parameter $\bar{\gamma}_\omega$ by evaluating eqn (3) in the limit $k_B T/\hbar\omega > 1$ as a function of an upper cut-off frequency ω'. In effect, we have computed the function

$$\bar{\gamma}_\omega(\omega') = \frac{\int_0^{\omega'} \gamma(\omega) g(\omega) \mathrm{d}\omega}{\int_0^{\omega'} g(\omega) \mathrm{d}\omega} \qquad (6)$$

where $\gamma(\omega)$ is the Grüneisen parameter and $g(\omega)$ is the vibrational density of states at frequency ω.

This function is shown in Fig. 7 where the key feature is the pair of negative peaks at low frequencies. The first, at ~0.25 THz, results from the contribution of the lower-frequency acoustic modes to the overall Grüneisen parameter. The second, at ~0.5 THz, results from the low-lying optic mode that undergoes little variation in frequency as a function of wave vector. Both modes clearly make the largest contribution to the negative value of the overall Grüneisen parameter. At higher frequencies, $\bar{\gamma}_\omega$ tends towards a smaller negative value as the contribution from phonons with large negative Grüneisen parameters is increasingly outweighed by higher-frequency phonons with smaller negative Grüneisen parameters as well as higher-frequency phonons with positive Grüneisen parameters.

3.2 Flexibility analysis

Since the full MOF-5 phonon spectrum is highly complex, we present in Fig. 8 a convenient visual representation of the different types of RUMs in the *ab initio* phonon spectrum by colouring the dispersion curves according to the value of the matching parameter $m_{i,\mathbf{k}}$ introduced in eqn (5). The values of $m_{i,\mathbf{k}}$ were converted to a two-dimensional linear colour scale such that the colour saturation ranges from white ($m_{i,\mathbf{k}} = 0$) through to full strength colour ($m_{i,\mathbf{k}} = 1$), with the colour

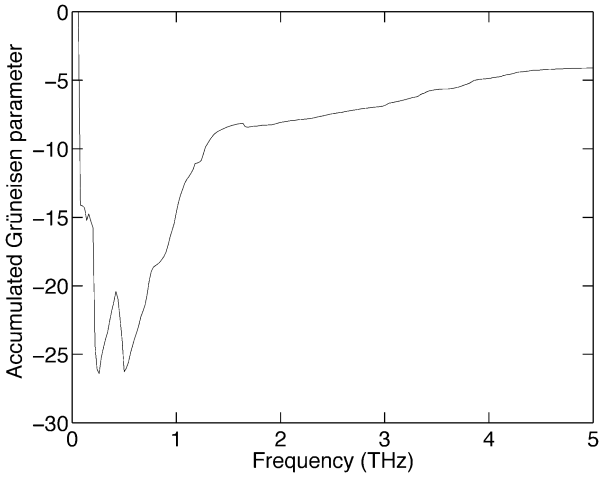

Fig. 7 Calculation of the overall Grüneisen parameter for all frequencies up to a maximum cut-off frequency, shown as a function of the cut-off frequency. Thus the value of the Grüneisen parameter at any value of the frequency arises solely from the set of modes of lower frequency. The negative peaks arise respectively from the acoustic modes without (~0.25 THz) and with (~0.5 THz) the contribution from the low-frequency optic modes.

depending on the form of the eigenvector of the flexibility model. RUMs involving only translations of rigid units are coloured blue and RUMs involving only rotations of rigid units are coloured red. RUMs that have mixed rotation/translation character are coloured purple, the exact ratio of red (rotation) and blue (translation) depending on their respective contribution.

Densities of states are also shaded using a simpler one-dimensional colour scale such that the shade of each bin ranges from white (average $m_{i,\mathbf{k}}$ for the bin is 0) through to black (average $m_{i,\mathbf{k}}$ for the bin is 1).

Fig. 8 shows separate representations for shaded phonon dispersion curves and densities of states for each of the six models, formed as the permutations of the representations of the flexibilities of the ligand and of the Zr_4O_{13} cluster. Here we present the results according to the flexibility of the ligand.

3.2.1 Rigid BDC rectangles. Results from $m_{i,\mathbf{k}}$ mapping for the two models with completely rigid BDC ligands are shown in the top row in Fig. 8. The model that treats the inorganic unit as a single rigid polyhedron is highly constrained. Only the acoustic phonons around Γ, corresponding to translations of the entire lattice, have large $m_{i,\mathbf{k}}$. There are also some optic modes with non-negligible values of $m_{i,\mathbf{k}}$ around 2.75 THz, but these are not a major factor in NTE. When the inorganic unit is instead treated as four separate rigid ZnO_4 tetrahedra, we find non-zero values of $m_{i,\mathbf{k}}$ for many of the phonons with frequencies in the range 0–2.75 THz. $m_{i,\mathbf{k}}$ is largest for the acoustic phonons for wave vectors along the direction Γ–X in reciprocal space. It also makes some non-trivial contribution to the strong NTE phonons of frequency 0.5 THz with wave vectors away from Γ as well as to the strong NTE phonons with frequency 1.6 THz at wave vectors close to Γ. Therefore, a model which combines motion of rigid ZnO_4 units with a rigid BDC rectangle describes the acoustic NTE phonons in MOF-5 for the Γ–X direction. This model also has some association with the strongest optic NTE phonons in MOF-5, without completely describing them.

3.2.2 Edge-sharing BDC rectangles. The results for the models that represent the BDC ligand as a set of three edge-sharing rectangles are shown in the middle row of Fig. 8. The model that treats the inorganic unit as a single rigid polyhedron has non-zero values of $m_{i,\mathbf{k}}$ for all phonons that are identified as NTE in Fig. 6. $m_{i,\mathbf{k}}$ rises to reach $\sim$1 for the strongest NTE phonons (with the exception of the acoustic phonon X–W). $m_{i,\mathbf{k}}$ is also $\sim$1 for the weak NTE phonons around 8 THz.

The rotational and translational components of $m_{i,\mathbf{k}}$ vary as a function of wave vector. However, the lowest frequency phonons remain primarily translational in nature whilst the higher frequency phonons have a larger rotational component.

The strong NTE optic mode at 0.5 THz must correspond to the previously-identified 'trampoline mode'[14] since this mode involves translation of the benzene ring out of the plane of the ligand. Higher frequency phonons are variations of this eigenvector in that they involve an additional energy cost due to rotation of components within the BDC ligand.

If the inorganic unit is instead treated as four separate rigid ZnO_4 tetrahedra, $m_{i,\boldsymbol{k}}$ values rise slightly in the 0–2.75 THz range, but the overall difference is negligible. Therefore, a model treating the ZnO_4 units as four separate tetrahedra along with the BDC ligand as edge-sharing rectangles, does not add any extra information to that already provided by less flexible models.

3.2.3 BDC 'bowtie'. The results for the two models that represent the BDC ligand as corner-sharing carboxylate triangles and a benzene hexagon (also known as a 'bowtie' model) are shown in the bottom row of Fig. 8. With the inorganic cluster treated as a rigid entity, we find $m_{i,\mathbf{k}} \approx 1$ for phonons with frequencies 0–1.6 THz and at 7.9 THz and non-zero values of $m_{i,\mathbf{k}}$ for phonons at 1.6–5.4 THz. However, once again, $m_{i,\mathbf{k}}$ is small for the strong acoustic NTE phonon in the X–W direction.

If the inorganic unit is treated as four separate rigid ZnO_4 tetrahedra, then values of $m_{i,\mathbf{k}}$ for phonons up to 2.75 THz are all approximately equal to 1. Once again, however, the acoustic NTE phonon X–W still has small $m_{i,\mathbf{k}}$.

Therefore, most of the lowest part of the frequency spectrum (including almost all non-trivial NTE phonons) can be described by a model involving rigid ZnO_4 tetrahedra and BDC 'bowties'. The very weak NTE phonons at 2.75–5.4 THz are partially described by such a model, but involve additional distortions of the crystal structure. Note that this model can also incorporate some motions that would not actively contribute to NTE, such as twisting of the benzene group about an axis along the length of the ligand. These motions appear to be mixed in with other, NTE-driving, motions in the real vibrational spectrum.

The extra degree of flexibility described by this model does not actually yield any additional insight into the strongest NTE phonons, but it does fill in many of the otherwise missing details relating to weaker NTE phonons at higher frequencies.

3.3 Visual analysis of acoustic modes at X

While the flexibility model analysis has allowed us to explain the majority of the low-frequency phonon spectrum of MOF-5, one important region remains unexplained. This is the acoustic phonon around the X–W region in reciprocal space which,

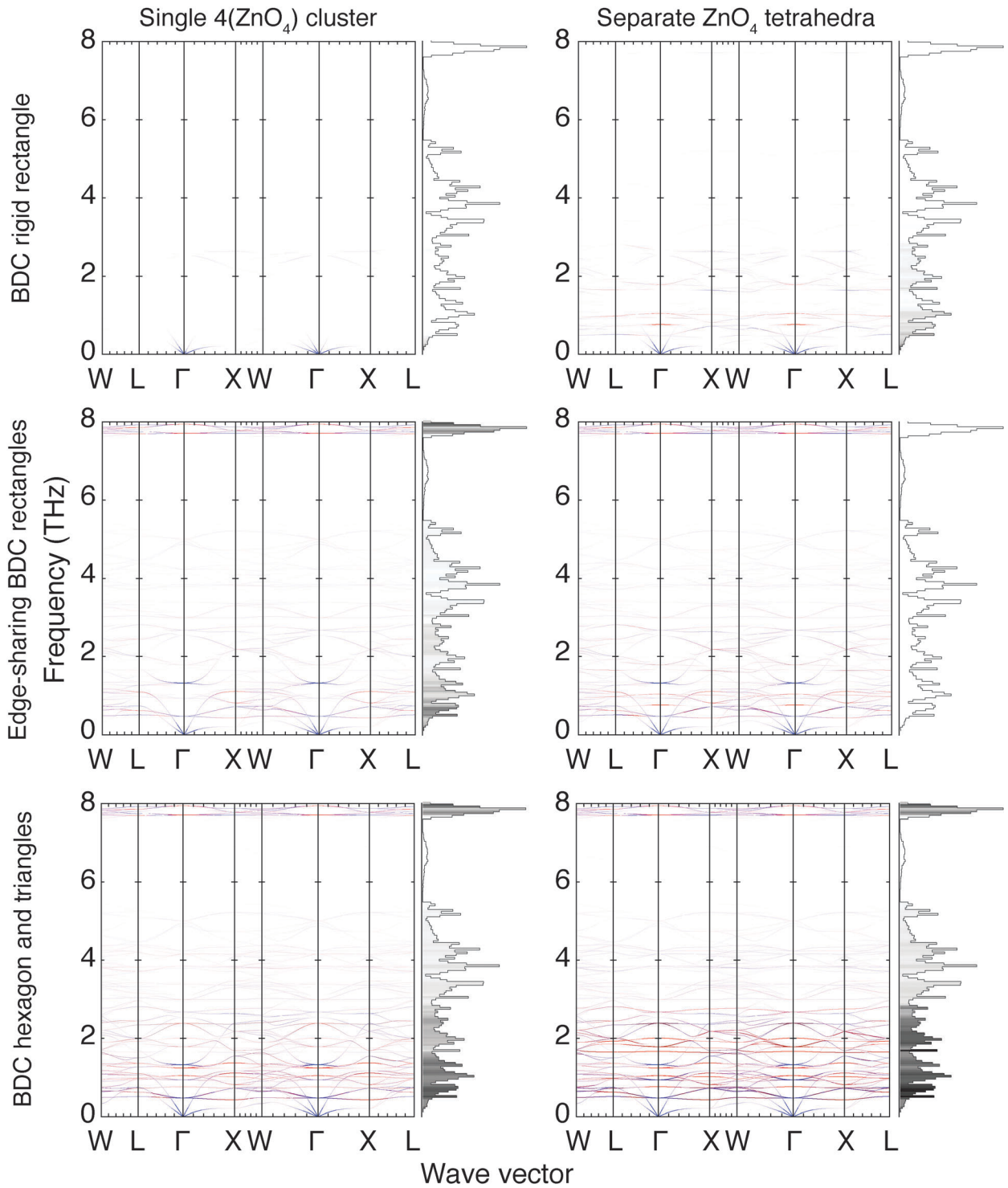

Fig. 8 Phonon dispersion curves and full Brillouin zone density of states for MOF-5. Wave vectors are labelled as in Fig. 6. The data are shaded according to the value of $m_{i,\mathbf{k}}$ of each mode at each wave vector. The strength of the colour used in the dispersion curves ranges from white ($m_{i,\mathbf{k}} = 0$) through to full strength colour ($m_{i,\mathbf{k}} = 1$). The colour itself ranges from blue to represent 100% polyhedral translations, through purple for modes of mixed rotation/translation character, to red representing 100% polyhedral rotations. The colour scale used in the densities of states ranges from white ($m_{i,\mathbf{k}} = 0$) through to black ($m_{i,\mathbf{k}} = 1$), with each bin in the density of states shaded according to the average value of $m_{i,\mathbf{k}}$ for each bin.

according to Fig. 6, makes a significant contribution to NTE but which, according to Fig. 8, cannot be described by any of the flexibility model investigated in this paper.

The eigenvector for the acoustic mode at wave vector X is shown in Fig. 9. It corresponds to a shear displacement of one layer relative to another whilst retaining the basic character of

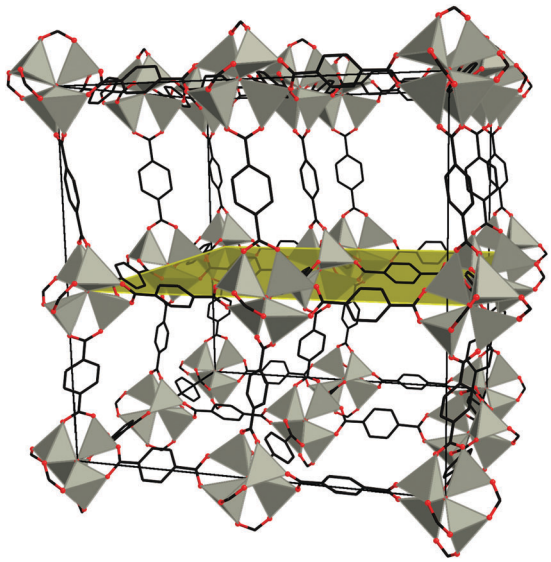

Fig. 9 Representation of the transverse acoustic mode at the X = (1,0,0) wave vector. This shows shearing of alternate layers (in contrast to the same mode at zero wave vector which corresponds to all layers moving in the same direction). The subtle bending of the ligands and ZnO_4 units pulls the layers together, and this contributes to NTE.

an acoustic mode. In the case of the mode at the X point, alternate layers move in opposite directions (note that, at zero wave vector, each layer would move in the same direction). The motion of the ligands with the shear pulls the connected layers together, thereby reducing the volume. At the X point this displacement can only be accomplished through a small distortion of the shape of the ligands and ZnO_4 tetrahedra in a manner not accounted for by the flexibility models discussed above.

3.4 Overview

In summary, phonons calculated for MOF-5 (without the inclusion of dispersion forces) show that NTE in this material is primarily driven by two mechanisms. The first is an acoustic phonon that drives strong NTE in the Γ–X–W region of the Brillouin zone which corresponds to motion of rigid BDC ligands and ZnO_4 tetrahedra in the Γ–X direction and to motion of near-rigid BDC ligands and ZnO_4 tetrahedra in the X–W direction. The second mechanism involves a very low frequency (0.5 THz) optic phonon that drives strong NTE across the Brillouin zone which corresponds to a 'trampoline mode' in the BDC ligand.

As frequency increases to 5.4 THz, NTE phonons continue to exist but become weaker as their mechanisms resemble trampoline mode-like flexing of BDC ligands but with increased deformation of the ligand itself.

Two other features within this frequency range (0.5–5.4 THz) merit mention. The first is another, as yet, uncharacterised (*i.e.* not explained by any flexibility model considered here) weak PTE phonon at 1.2 THz. The second is a strong NTE phonon at 1.6 THz that corresponds to a trampoline-like phonon that minimises deformation of the BDC ligand but which involves increased motion of ZnO_4 tetrahedra within the inorganic unit.

Phonons that involve non-trivial amounts of bond stretching drive weak PTE in the 5.4–7.9 THz range. Finally, there is a narrow band of weak NTE phonons around ~7.9 THz that correspond to a trampoline-like motion but involve an extra deformation of the BDC unit, albeit without significant deformation of the carboxylate or benzene groups.

Phonons above this frequency all involve non-trivial levels of bond stretching and thus drive PTE.

4 Discussion

Our investigation finds that an acoustic phonon with a mechanism not previously documented (motion of rigid or near-rigid BDC ligands and ZnO_4 tetrahedra) makes a sizeable contribution to the overall NTE in MOF-5. Specifically, NTE in MOF-5 is driven by two types of phonon, one of which is this hitherto unidentified acoustic NTE phonon that spans the Γ–X–W region of reciprocal space. In the Γ–X direction this acoustic phonon can be described by translations of a rigid BDC ligand bonded to individual rigid ZnO_4 tetrahedra; in the X–W direction the BDC ligands and ZnO_4 tetrahedra undergo some minor distortion.

The second type of phonon responsible for driving much of the NTE in MOF-5 is the optic 'trampoline' mode that spans the entire Brillouin zone. In this respect this study is, therefore, in accordance with previous work that identified the significant contribution of the trampoline mode in MOF-5 to its NTE. There are also much smaller contributions to NTE from phonons up to 5.4 THz and in a narrow band around 7.9 THz. These modes generally represent variations of the trampoline mode (with additional, higher frequency, deformations of the BDC ligand). They also incorporate some motions that cannot actively contribute to NTE, such as twisting of the benzene group about an axis along the length of the ligand.

Acoustic phonons have been shown to play a critical role in driving the NTE of other materials such as $Zn(CN)_2$[6] and Cu_2O.[17,32] In general, however, the role of acoustic modes is rarely evaluated in published studies of NTE phonons; most studies to date have tended to limit their focus to the contributions of optic modes only. This is primarily due to practical difficulties in observing acoustic phonons experimentally. However, in order to truly capture the behaviour of an NTE material, one cannot afford to rule out the importance of acoustic phonons.

Two important issues remain less understood. The first relates to the acoustic mode in the X–W direction, which makes a strong contribution to NTE but whose mode eigenvectors involve distortions of the ligands and ZnO_4 tetrahedra and thus do not readily map onto the flexibility modes investigated here. The observed distortions are minor (explaining why the frequencies of these phonons are not large) but, nevertheless, one might not have expected to see any noticeable distortion of these structural units at such low energies. The second issue relates to the single weak PTE phonon at 1.2 THz. This did not generate any remarkable features in the flexibility mapping but,

rather, it appeared to share the same features of surrounding NTE phonons.

Acknowledgements

This work was supported by NERC and CrystalMaker Software Ltd. (LHNR). Via our membership of the UK's HPC Materials Chemistry Consortium, which is funded by EPSRC (EP/F067496), this work made use of the facilities of HECToR, the UK's national high-performance computing service, which is provided by UoE HPCx Ltd at the University of Edinburgh, Cray Inc and NAG Ltd, and funded by the Office of Science and Technology through EPSRC's High End Computing Programme.

References

1 C. Lind, *Materials*, 2012, **5**, 1125–1154.
2 C. P. Romao, K. J. Miller, C. A. Whitman, M. A. White and B. A. Marinkovic, in *Comprehensive Inorganic Chemistry II*, ed. J. Reedijk and K. Poeppelmeier, Elsevier, Amsterdam, 2nd edn, 2013, ch. 4.07 – Negative Thermal Expansion (Thermomiotic) Materials, pp. 127–151.
3 P. R. L. Welche, V. Heine and M. T. Dove, *Phys. Chem. Miner.*, 1998, **26**, 63–77.
4 V. Heine, P. R. L. Welche and M. T. Dove, *J. Am. Ceram. Soc.*, 1999, **82**, 1793–1802.
5 A. L. Goodwin and C. J. Kepert, *Phys. Rev. B: Condens. Matter Mater. Phys.*, 2005, **71**, 140301.
6 H. Fang, M. T. Dove, L. H. N. Rimmer and A. J. Misquitta, *Phys. Rev. B: Condens. Matter Mater. Phys.*, 2013, **88**, 104306.
7 H. Li, M. Eddaoudi, M. O'Keeffe and O. M. Yaghi, *Nature*, 1999, **402**, 276–279.
8 W. Zhou, H. Wu, T. Yildirim, J. R. Simpson and A. R. H. Walker, *Phys. Rev. B: Condens. Matter Mater. Phys.*, 2008, **78**, 054114.
9 M. T. Dove, *Introduction to lattice dynamics*, Cambridge University Press, Cambridge, 1st edn, 1993, vol. 4.
10 A. P. Giddy, M. T. Dove, G. S. Pawley and V. Heine, *Acta Crystallogr., Sect. A: Found. Crystallogr.*, 1993, **49**, 697–703.
11 K. D. Hammonds, M. T. Dove, A. P. Giddy, V. Heine and B. Winkler, *Am. Mineral.*, 1996, **81**, 1057–1079.
12 A. L. Goodwin, *Phys. Rev. B: Condens. Matter Mater. Phys.*, 2006, **74**, 134302.
13 N. Lock, Y. Wu, M. Christensen, L. J. Cameron, V. K. Peterson, A. J. Bridgeman, C. J. Kepert and B. B. Iversen, *J. Phys. Chem. C*, 2010, **114**, 16181–16186.
14 N. Lock, M. Christensen, Y. Wu, V. K. Peterson, M. K. Thomsen, R. O. Piltz, A. J. Ramirez-Cuesta, G. J. McIntyre, K. Noren, R. Kutteh, C. J. Kepert, G. J. Kearley and B. B. Iversen, *Dalton Trans.*, 2013, **42**, 1996–2007.
15 W. Zhou and T. Yildirim, *Phys. Rev. B: Condens. Matter Mater. Phys.*, 2006, **74**, 180301.
16 T. Yildirim and M. R. Hartman, *Phys. Rev. Lett.*, 2005, **95**, 215504.
17 L. H. N. Rimmer, M. T. Dove, B. Winkler, D. J. Wilson, K. Refson and A. L. Goodwin, *Phys. Rev. B: Condens. Matter Mater. Phys.*, 2014, **89**, 214115.
18 S. J. Clark, M. D. Segall, C. J. Pickard, P. J. Hasnip, M. I. J. Probert, K. Refson and M. C. Payne, *Z. Kristallogr. – Cryst. Mater.*, 2005, **220**, 567–570.
19 J. P. Perdew, K. Burke and M. Ernzerhof, *Phys. Rev. Lett.*, 1996, **77**, 3865–3868.
20 J. P. Perdew, K. Burke and M. Ernzerhof, *Phys. Rev. Lett.*, 1997, **78**, 1396.
21 S. Grimme, *J. Comput. Chem.*, 2006, **27**, 1787–1799.
22 K. Refson, P. R. Tulip and S. J. Clark, *Phys. Rev. B: Condens. Matter Mater. Phys.*, 2006, **73**, 155114.
23 H. J. Monkhorst and J. D. Pack, *Phys. Rev. B: Condens. Matter Mater. Phys.*, 1976, **13**, 5188–5192.
24 M. I. Aroyo, J. M. Perez-Mato, D. Orobengoa, E. Tasci, G. de la Flor and A. Kirov, *Bulg. Chem. Commun.*, 2011, **43**, 183–197.
25 M. I. Aroyo, J. M. Perez-Mato, C. Capillas, E. Kroumova, S. Ivantchev, G. Madariaga, A. Kirov and H. Wondratschek, *Z. Kristallogr. – Cryst. Mater.*, 2006, **221**, 15–27.
26 M. I. Aroyo, A. Kirov, C. Capillas, J. M. Perez-Mato and H. Wondratschek, *Acta Crystallogr., Sect. A: Found. Crystallogr.*, 2006, **62**, 115–128.
27 E. S. Tasci, G. de la Flor, D. Orobengoa, C. Capillas, J. M. Perez-Mato and M. I. Aroyo, EPJ Web of Conferences, 2012.
28 *Bilbao Crystallographic Server*, Last accessed 24th October 2013. http://www.cryst.ehu.es.
29 V. I. Hegde, J.-C. Tan, U. V. Waghmare and A. K. Cheetham, *J. Phys. Chem. Lett.*, 2013, **4**, 3377–3381.
30 K. D. Hammonds, M. T. Dove, A. P. Giddy and V. Heine, *Am. Mineral.*, 1994, **79**, 1207–1209.
31 C. Bradley and A. Cracknell, *The Mathematical Theory of Symmetry in Solids: Representation Theory for Point Groups and Space Groups*, Oxford University Press, 1972.
32 K.-P. Bohnen, R. Heid, L. Pintschovius, A. Soon and C. Stampfl, *Phys. Rev. B: Condens. Matter Mater. Phys.*, 2009, **80**, 134304.

